Finite Strain Calculations of Continental Deformation
1. Method and General Results for Convergent Zones

GREGORY HOUSEMAN

Research School of Earth Sciences, Australian National University, Canberra

PHILIP ENGLAND

Department of Geological Sciences, Harvard University, Hoffman Laboratory, Cambridge, Massachusetts

A finite element method is used to calculate stresses and strain rates in a thin viscous sheet, representing the continental lithosphere, that is bordered in one part by an indenting boundary. We calculate solutions for velocity fields, crustal thickness distributions, strain rates, rotation (time-integrated vorticity), and finite strain ellipsoids to show the dependence of these quantities on the controlling parameters: the stress-strain exponent n and the strength of the sheet relative to the gravitational forces (which may be expressed as a dimensionless number: the Argand number Ar). For $n > 3$ and Ar between 1 and 10 a plateau of thickened crust is formed in front of the indenter. The strain histories of individual elements within the viscous sheet may be quite complex, and the finite strain at the end of deformation may bear no obvious relation to the principal stress orientations during the deformation. The strain rate fields are interpreted in terms of the style of faulting that would be expected in the brittle upper crust if it were coupled to the ductile, but stronger, upper mantle. In general, the length scale of deformation increases with Ar and time since the start of the collision and decreases with n; for $Ar \gtrsim 3$, the increase in length scale is accompanied by a change in the style of deformation: from predominantly crustal thickening (with thrust faulting in the brittle layer) to predominantly transcurrent deformation (strike-slip faulting in the brittle layer).

1. INTRODUCTION

It has been recognized for several years that the deformation of the continents represents a significant departure from the rules of plate tectonics, and several authors [e.g., *Molnar et al.*, 1973; *Molnar and Tapponnier*, 1975; *McKenzie*, 1976] have drawn attention to the distributed and diffuse nature of the present-day deformation of the continents. This recognition has led to the investigation of continental deformation in terms of mechanics of a continuous medium [e.g., *Tapponnier and Molnar*, 1976; *Bird and Piper*, 1980; *England and McKenzie*, 1982; *Vilotte et al.*, 1982].

The collision between India and Asia is the largest present-day example of continental deformation [*Molnar and Tapponnier*, 1975] and has consequently received the most attention. Previous calculations for this collision have been carried out for infinitesimal [*Tapponnier and Molnar*, 1976] or small [*Vilotte et al.*, 1982] strains or have neglected vertical strain [*Tapponnier and Molnar*, 1976], the influence of gravity acting on crustal thickness contrasts [*Vilotte et al.*, 1982], or the influence of a moving boundary on the continental lithosphere [*England and McKenzie*, 1982]. In addition, these studies have tended to concentrate on the crustal thickness distribution, and there has not been a quantitative treatment of other features of the deformation, such as the stress and strain rate fields, finite strain, latitudinal displacements, and finite rotations, all of which are potential tests of models for continental deformation.

The purpose of this paper is to perform numerical experiments on a rheologically simple continuum model for the continental lithosphere that is not subject to the limitations mentioned above; to discuss the calculated distribution of stresses, strain rates, and strain; and to relate these to the styles of discontinuous deformation (faulting) that might be expected in the near-surface portions of the deforming continental lithosphere.

The aim of such an investigation is to attempt a better understanding of the dynamics of continental deformation in general and, in particular, to compare the calculated results with the observations in an active convergence zone of central Asia. The comparison is left to the companion paper [*England and Houseman*, this issue] because while the surface elevation in Asia is quite well known, the other parameters of deformation are sparsely sampled over an area of more than 2000×2000 km and are often the subject of debate. In contrast, the results of the numerical experiments described in this paper follow directly once the assumptions have been stated and the boundary conditions chosen.

2. DESCRIPTION OF THE MODEL

We use the thin viscous shell formulation of *England and McKenzie* [1982] and adopt finite element techniques similar to those described by *Bird and Piper* [1980] and *Bird and Baumgardner* [1984] to solve the governing equations (Appendix B). The assumptions involved in the thin viscous sheet model are discussed in detail by *Bird and Piper* [1980] and *England and McKenzie* [1982], so we only summarize them here. The continental lithosphere is assumed to behave, over long time intervals, as a continuous medium deforming by steady state creep. Because the Reynolds number is negligible, the inertial terms disappear from the force balance:

$$\frac{\partial \sigma_{ij}}{\partial x_j} = \rho g a_i \tag{1}$$

where $a = (0, 0, 1)$, g is the acceleration due to gravity, ρ is the density, and σ_{ij} is the (i, j)th component of the stress tensor. The flow is assumed to be incompressible in three dimensions, so

$$\nabla \cdot \mathbf{u} = 0 \tag{2}$$

(where $\mathbf{u} = (u, v, w)$ is the velocity vector). These, with a rheological relation between stresses and strain rates, constitute

four equations in four unknowns: the velocity components and the pressure. In the thin sheet approximation it is assumed that the top and base of the continental lithosphere are free of tractions and that the lateral gradients of loads acting on the lithosphere are small. This approximation permits calculations to be carried out in terms of vertical averages of stress and strain rate, and reduces (1) and (2) to three equations in three unknowns: the horizontal velocity components and the crustal thickness. The crustal thickness is specified initially, and its variation in time then follows directly from the strain rate field by the continuity equation (2) (see Appendix B).

In this paper we have chosen to use a vertically averaged power law rheology for the continental lithosphere (equation (3)). Several authors have used a combination of plastic and viscous rheologies [e.g., Bird and Piper, 1980; Bird and Baumgardner, 1984; Vilotte et al., 1982], reflecting the belief that friction on faults and/or plastic failure in the upper lithosphere play an important role in governing the vertically averaged rheology of the continental lithosphere. We agree that this is likely but do not feel that the current state of knowledge permits a unique choice of a vertically averaged rheology based on a specified distribution of deformation mechanism with depth; the principal uncertainties are the temperature distribution in the lithosphere and flow laws for crustal materials. However, the vertically averaged stress-strain rate relations for continental lithosphere containing the kind of rheological layering discussed by Brace and Kohlstedt [1980] may be approximated over a geologically relevant range of strain rates (say 10^{-13} to 10^{-17} s^{-1}) by a rheology of the form commonly assumed for a shear-thinning fluid, that depends only on the two parameters, B and n:

$$\bar{\tau}_{ij} = B\dot{E}^{(1/n-1)}\dot{\varepsilon}_{ij} \qquad (3)$$

where $\bar{\tau}_{ij}$ are the vertically averaged components of the deviatoric stress tensor and the strain rates $\dot{\varepsilon}_{ij}$ are defined in terms of the velocity gradients,

$$\dot{\varepsilon}_{ij} = \frac{1}{2}\left(\frac{\partial u_i}{\partial x_j} + \frac{\partial u_j}{\partial x_i}\right) \qquad (4)$$

and

$$\dot{E} = (\dot{\varepsilon}_{ij}\dot{\varepsilon}_{ij})^{1/2} \qquad (5)$$

B is a constant that depends on the vertically integrated structure of the lithosphere. A stress-strain exponent n of 3 would be appropriate for a lithosphere whose vertically averaged rheology is dominated by the power law creep of olivine [e.g., Goetze, 1978], while a higher value of n would be a better approximation to a lithosphere governed by the high stress plasticity of olivine [e.g., Ashby and Verrall, 1978; Goetze, 1978] or one in which friction on faults contributed significantly to its vertically averaged strength. A rheology with $n > 3$ thus represents a vertical average of more than one deformation mechanism; the value of the stress-strain exponent does not represent any single physical process (see Sonder and England [1986] for further discussion).

In this paper we present the results of experiments where the power law exponent varies between $n = 1$ (Newtonian fluid) and $n = 10$; at the higher end of this range the dependence of strain rate on stress is so high that although the fluid does not have a yield stress like a perfectly plastic substance, it can go from a regime in which it is deforming at a geologically negligible rate to one of substantial strain rates over a small stress interval.

Aside from the boundary conditions, which are shown in Figure 1 for the two different cases investigated here, there are
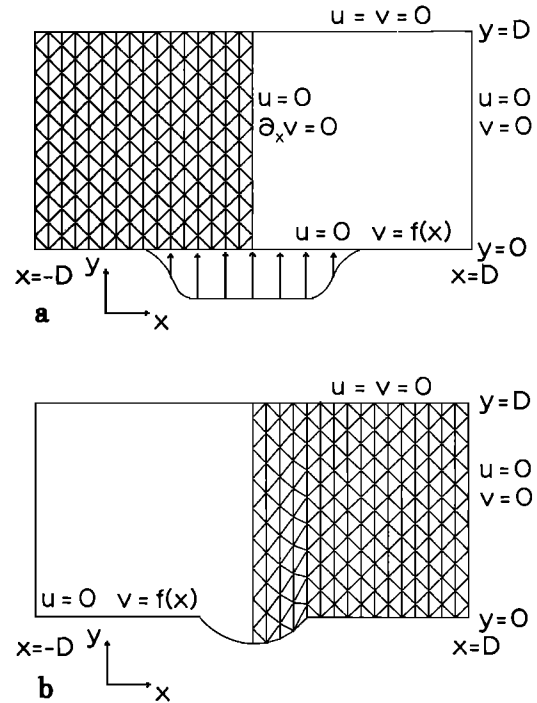

Fig. 1. Configuration, coordinates, and boundary conditions for the numerical experiments. The figures to follow show the right half of the symmetric solutions. The regions are divided into triangular elements by the meshes shown, and nodal points are found at the vertices and midpoints of each triangle. The indenter is described by the dimensionless velocity function $f(x)$ on the boundary $y = 0$, where $f(x) = 0$ for $D/2 \le |x| \le D$, $f(x) = 1$ for $0 \le |x| \le D/4$, and $f(x) = \cos^2 [2\pi(x/D - 1/4)]$ for $D/4 \le |x| \le D/2$.

two parameters that control the flow; the stress-strain exponent n in the power law rheology and the Argand number [England and McKenzie, 1982] (see equation (B1)). The Argand number may be written

$$Ar = \frac{g\rho_c(1 - \rho_c/\rho_m)L}{B(V_0/L)^{1/n}} \qquad (6)$$

where g is the gravitational acceleration, L is the thickness of the thin sheet, V_0 is the indentation velocity (Figure 1), and ρ_c and ρ_m are the densities of crust and mantle layers, respectively. The numerator may be thought of as proportional to the vertically averaged deviatoric stress due to a crustal thickness contrast of magnitude L, and the denominator is the vertically averaged deviatoric stress required to deform the medium at the nominal strain rate: the collision velocity divided by the lithosphere thickness. As the numerator is fairly well constrained in the case we consider, the Argand number is a measure of the vertically averaged strength of the continental lithosphere. The governing equations for the thin sheet [England and McKenzie, 1982] are given in Appendix B, along with a summary of the means of solution.

3. RESULTS

Numerical experiments were carried out with the domains of solution and boundary conditions shown in Figure 1, with values of 1, 3, and 10 for the stress exponent n and Argand numbers between 0 and 30. Dimensional quantities are calculated using the parameters listed in Table 1. The stress-strain rate coefficient B can be obtained from equation (6) for given n and Ar. The calculations were generally stopped at the point where the indenter had moved two fifths of the way across the

TABLE 1. Nominal Values of the Physical Constants, as Used in the Calculation

	Value
g	$10 \ \mathrm{m/s^2}$
L	$100 \ \mathrm{km}$
D	$5000 \ \mathrm{km}$
V_0	$50 \ \mathrm{mm/yr}$
S_0	$35 \ \mathrm{km}$
ρ_m	$3.27 \times 10^3 \ \mathrm{kg/m^3}$
ρ_c	$2.80 \times 10^3 \ \mathrm{kg/m^3}$

box, because this point corresponds roughly to the configuration of the present-day collision of India with Asia (a displacement of 2000 km in 40 m.y. for the parameter values of Table 1). To determine whether the shape of the indenting boundary has a significant effect on the internal deformation of the sheet, we have used the two different boundary configurations shown in Figure 1.

3.1. Velocity Fields

England et al. [1985] derive approximate solutions for the velocity field in a thin viscous sheet subjected to a simplified boundary condition in which the velocity varies sinusoidally. We show here that these approximate solutions are also useful for describing the deformation of a viscous sheet subject to more geologically reasonable boundary conditions. England et al. [1985, equation (29)] give an expression for the y velocity (in the configuration of Figure 1) in regions where the x velocity is small (immediately in front of the indenter):

$$v \approx V_0 \cos \ (\pi x/D) e^{-(n)^{1/2}\pi y/2D} \qquad (7)$$

where n is the power law exponent (equation (3)), the dominant wavelength in the boundary condition of Figure 1 is
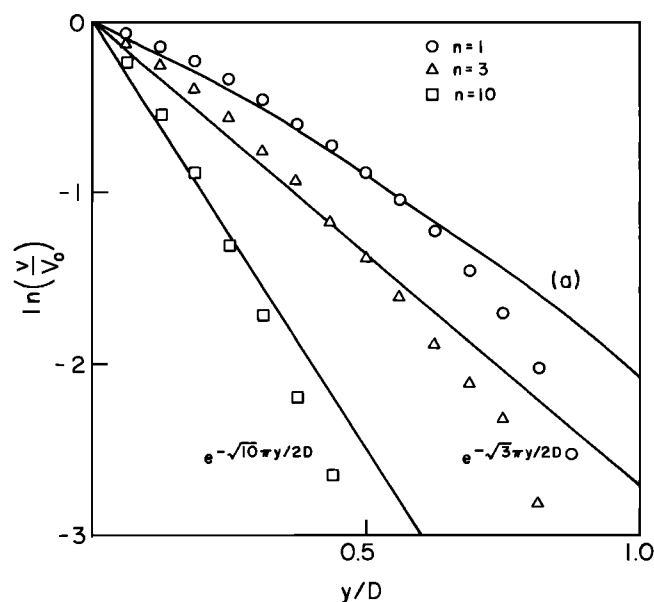

Fig. 2. The y velocities at $t' = 0$ on the plane $x = 0$, calculated on the finite element grid of Figure 1a for three different values of n. Symbols are plotted for each nodal point on the y axis (see Figure 1). The solid lines correspond to the exact ($n = 1$, curve a [England et al., 1985, equation (12)]) and approximate ($n = 3$, 10 [England et al., 1985, equation (29)]) solutions of England et al. [1985] for the deformation of a semi-infinite thin viscous sheet subject to the velocity boundary condition on $y = 0$: $u = 0$, $v = V_0 \cos \ (\pi x/D)$.

equal to $2D$, and V_0 is the maximum velocity on the influx boundary.

Figure 2 shows the y velocity calculated on the y axis (Figure 1a) at time zero for viscous sheets with power law exponents of $n = 1$, $n = 3$, and $n = 10$, compared with the simple approximation given in equation (7). It can be seen that the numerical solutions agree well with the analytical approximations. This allows us to identify a length scale for the compressive deformation in a zero Argand number sheet: according to the approximate relation of equation (7), the deformation produced by the velocity boundary conditions dies out with a scale length (or e-folding length) of approximately $2D/(n)^{1/2}\pi$, which is $0.64D$ for $n = 1$, $0.37D$ for $n = 3$, and $0.20D$ for $n = 10$.

Particularly when $n > 1$, the deformation immediately in front of the indenter is almost pure compression in the y direction accompanied by crustal thickening; consequently, provided the Argand number is small, the widths of regions of substantial increase in crustal thickness bear the same relation to n as do the velocity fields. This similarity of length scales may be seen in Figure 3, which compares the velocity and vertical strain rates at the beginning and after 24 m.y. of deformation for three experiments, with $n = 1$, $n = 3$, and $n = 10$, each with $Ar = 0$ and with the boundary conditions of Figure 1a. Figure 3 also shows that the across-strike width of the compressional deformation is unaffected by the finite displacement of the indenting boundary, so the approximation of equation (7) is likely to hold under a wide range of boundary conditions provided the Argand number is small.

3.2. Crustal Thickness, Strain Rate Fields, and Driving Forces for $Ar > 0$

In this section we show the influence of Argand number on crustal thickness as a function of time and compare these results with the crustal thicknesses calculated by England and McKenzie [1982] for a fixed boundary with an advected flux. Our results differ from those of England and McKenzie in ways that are important for quantitative comparisons between calculation and observation. The main consequence of using the more geologically realistic boundary condition is that the across-strike (y direction) width of the deformation is diminished because the region of thickest crust is kept close to the indenter rather than being advected into the interior [England and McKenzie, 1982, pp. 307–308]. This produces a more plateaulike form to the topography (Figure 4) than is the case for a fixed boundary; in turn, this affects the form of the strain rate field (Figure 5).

Figure 4 compares the crustal thickness distributions, after 40 m.y. of convergence, for experiments with $n = 3$, 10 and $Ar = 1$, 3, 10 for the two boundary conditions illustrated in Figure 1. The comparison for $n = 10$ between crustal thickness distribution for the straight indenter (Figures 4b, 4e, and 4h) and the arcuate indenter (Figures 4c, 4f, and 4i) shows that the important control on the shape of the thickened region is the location of the stress concentrations at the corners of the indenter. Outside the region enclosed by the arcuate boundary segment and the alternative straight boundary segment, the solutions for respective n and Ar are very similar, but the arcuate boundary produces a wider plateau of thickened crust in front of the indenter. However, variation of n and Ar results in much greater changes to the overall distribution of deformation.

The influence of the crustal thickness variation on the strain rate field can be seen in Figure 5, where contours of the vertical strain rate (thickening or thinning rate) are plotted for different values of Ar and n and the boundary conditions of
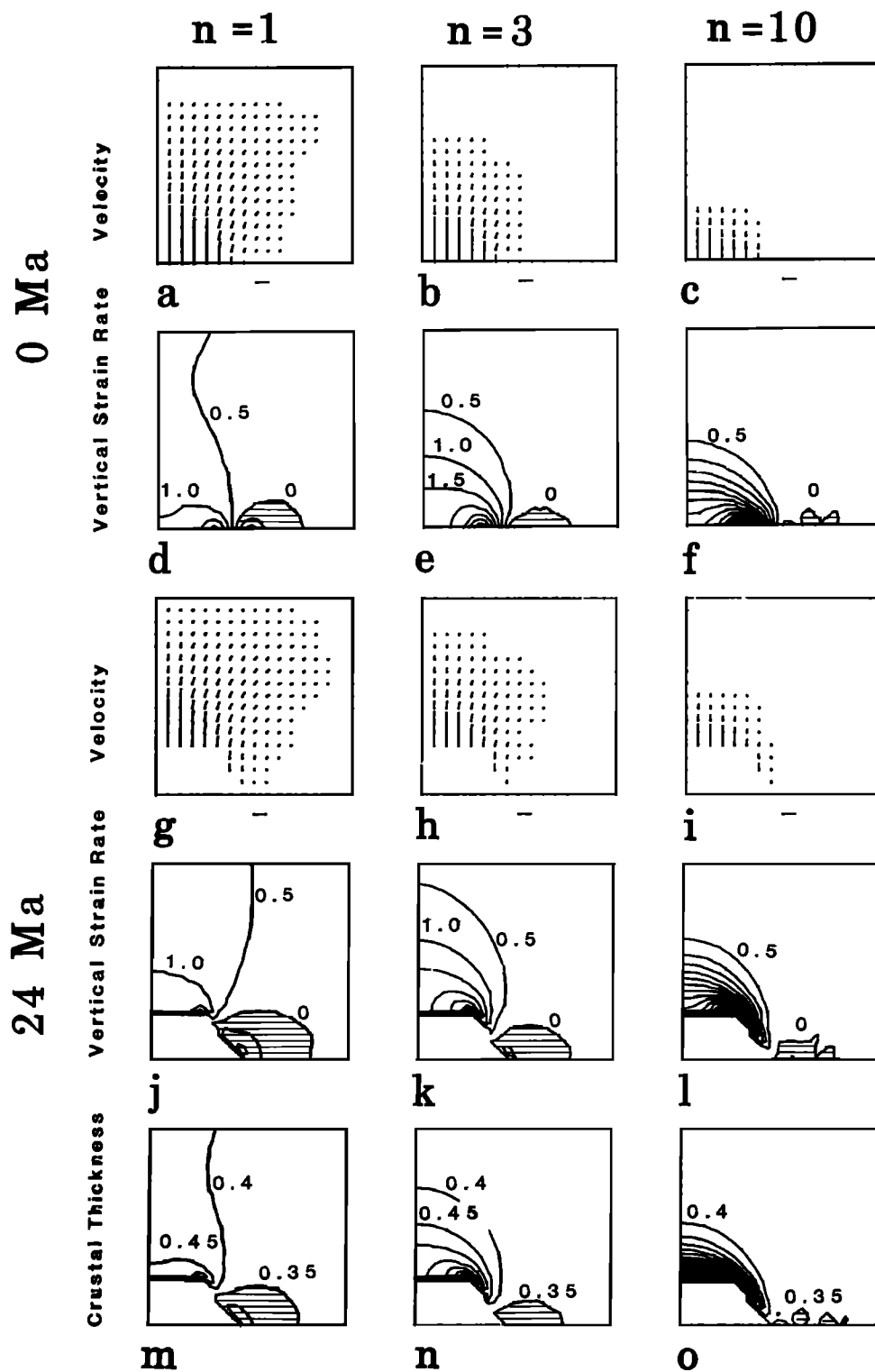
n = 1   n = 3   n = 10

Fig. 3. Velocity field for $t = 0$ (Figures $3a-3c$) and $t = 24$ Ma (Figures $3g-3i$), vertical strain rate for $t = 0$ (Figures $3d-3f$) and $t = 24$ m.y. (Figures $3j-3l$), and crustal thickness at $t = 24$ m.y. (Figures $3m-3o$). $Ar = 0$ in all cases and $n = 1$ for (Figures $3a$, $3d$, $3g$, $3j$, and $3m$), $n = 3$ for (Figures $3b$, $3e$, $3h$, $3k$, and $3n$), and $n = 10$ for (Figures $3c$, $3f$, $3i$, $3l$, and $3o$). Contour interval for $\dot{\varepsilon}_{zz}$ is 0.5 nondimensional units (equation (B3)) and for S is $0.05L$. Zones of crustal thinning ($\dot{\varepsilon}_{zz} < 0$) are shaded; similarly, the region of crustal thickness $S < 0.35L$ is shaded. S and $\dot{\varepsilon}_{zz}$ increase monotonically toward the corner of the indenter. For this and all subsequent plots, contours, stresses, and velocities are plotted after interpolation from the finite element mesh onto a net of points with equal x and y spacing. For contour plots, this spacing is $D/32$.

Figure 1; again, substantially similar results are obtained for the differently shaped boundaries (Figures 5c and 5h). At small time (and for all time when $Ar = 0$; see Figure 3) the deformation is concentrated near the indenter and more so as n is increased. However, when $Ar > 1$, there is a progressive outward migration, relative to the advancing indenter, of an arcuate zone in which the rate of crustal thickening is a local maximum. This arcuate zone overlaps the downward slope of
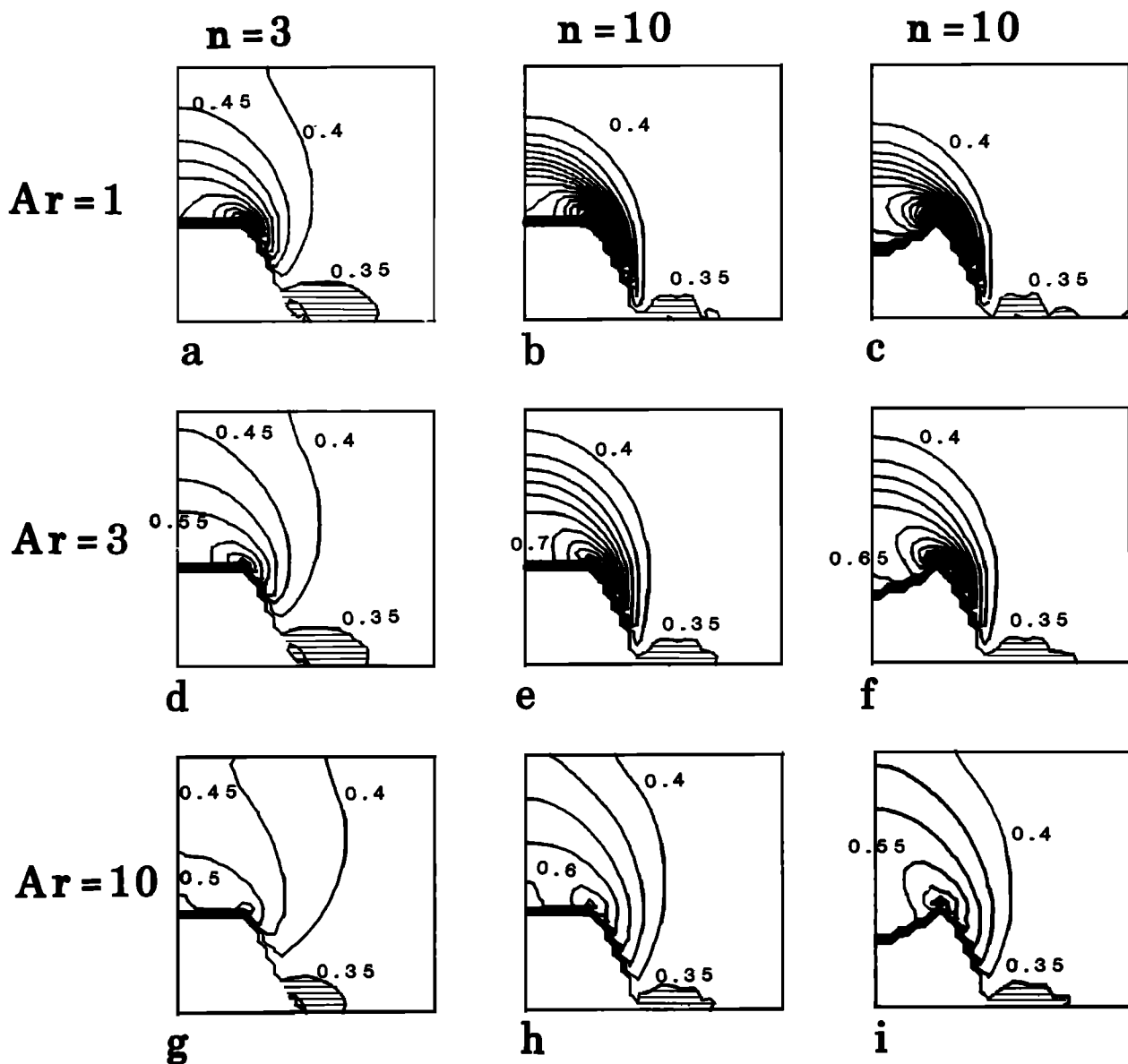
Fig. 4. Contours of crustal thicknesses at 40 m.y. for sheets having stress-strain exponents of 3 (Figures 4a, 4d, and 4g) and 10 (Figures 4b, 4c, 4e, 4f, 4h, and 4i). Boundary conditions are those of Figure 1a (Figures 4a, 4b, 4d, 4e, 4g, and 4h) and Figure 1b (Figures 4c, 4f, and 4i). Crustal thickness is contoured in units of 0.05L, and areas having crustal thickness less than the original (0.35L) are shaded. The Argand number for these calculations are 1 (Figures 4a–4c), 3 (Figures 4d–4f) and 10 (Figures 4g–4i).

the region of thickened crust; within this region the buoyancy forces resist further crustal thickening, so the zone of most rapid thickening is forced outward from the indenter. This is illustrated as a time progression in Figures 5a–5c for $n = 10$, $Ar = 3$, and the variation of the vertical strain rate field at $t = 40$ m.y. with n and Ar is shown in Figures 5d–5i.

The outward migration of crustal thickening differs significantly from the deformation described by *England and Mc-Kenzie* [1982] and from the deformation that is calculated from a thin viscous sheet model that neglects buoyancy (cf. Figures 3j–3l and *Vilotte et al.* [1982]).

Table 2 lists the average shear stress, $(\sigma_{xx} - \sigma_{zz})/2$, in the fluid immediately in front of the center of the indenter after 40 m.y. of convergence, for calculations with different combinations of Ar and n; the dimensional quantities are calculated using the parameter values given in Table 1.

3.3. Stress Fields, Fault Orientations, Rotations, and Finite Strains

The presence of numerous faults in the upper crust ensures that it is anisotropic and inhomogeneous, but without a knowledge of the initial distribution of these faults or of their development during the strain, it is impossible to account in detail for such features. In relating the deformation of the upper crust to that of the underlying lithosphere we shall make the assumption that is often explicitly or implicitly made in the discussion of intracontinental seismicity: that the continental crust contains sufficient randomly oriented preexisting faults that (on the scale that we can resolve in these calculations, ~200 km) the response to the stress field is approximately isotropic.

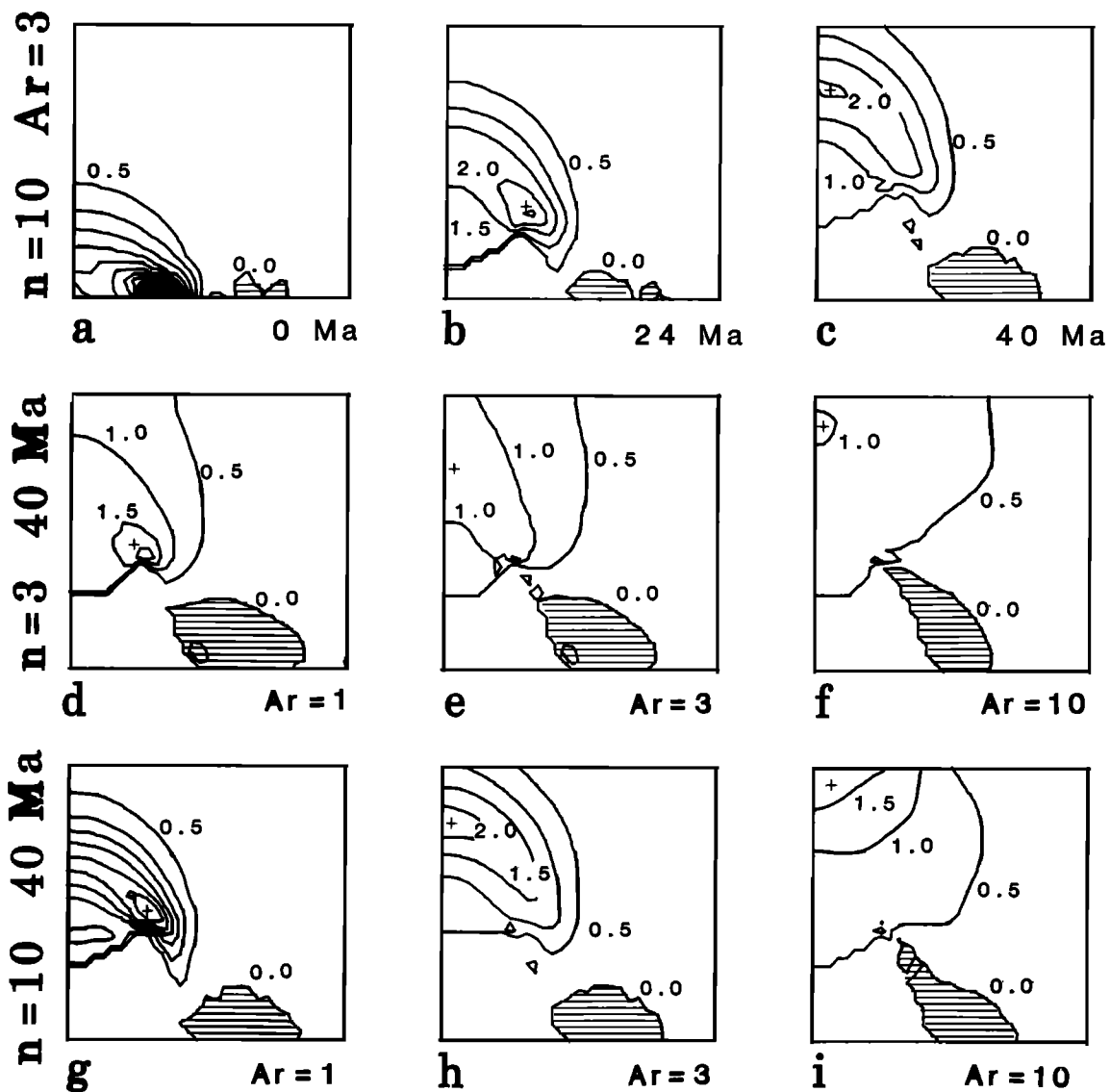*Stress fields and style of faulting.* We assume that the strain

Fig. 5. Contours of vertical strain rate for (Figures 5a-5c) $n = 10$, $Ar = 3$ and (a) $t = 0$ m.y., (b) $t = 24$ m.y., (c) $t = 40$ m.y. (Figures 5d-5f) $n = 3$, $t = 40$ m.y. and (d) $Ar = 1$, (e) $Ar = 3$, (f) $Ar = 10$; (Figures 5g-5i) $n = 10$, $t = 40$ m.y. and (g) $Ar = 1$, (h) $Ar = 3$, (i) $Ar = 10$. Boundary conditions of Figure 1b in all cases except Figure 5h which would otherwise duplicate Figure 5c. Local maxima in $\dot{\varepsilon}_{zz}$ are marked with a plus. Contour interval is 0.5 dimensionless units (equation (B3)).

TABLE 2. Plateau Crustal Thicknesses and Deviatoric Stresses

n	Argand Number	Plateau Crustal Thickness, km	Deviatoric Stress, MPa
1	0	52	...
3	0	64	176
3	3	55	54
3	10	49	14
5	1	66	284
5	3	59	90
10	1	74	400
10	3	63	130
10	10	54	38

Plateau crustal thickness is taken to be the maximum value of the crustal thickness on the y axis after 40 m.y. Deviatoric stress is $(\tau_{xx} - \tau_{zz})/2$ evaluated at the center of the indenter for the boundary conditions of Figure 1b. Dimensional stresses are undefined for $Ar = 0$.

rate field in the brittle crust is the same as calculated for the viscous layer; a triaxial strain increment can be accommodated by motion on two sets of fault planes; thus the strain rate tensor at a given point can be interpreted in terms of the style (thrust, normal, strike-slip, or combination) and magnitude (rate of moment release) of the expected faulting (Appendix A).

Figure 6 shows the calculated principal horizontal stresses for experiments with different n and Ar, upon which are superimposed the boundaries of regions in which the style of faulting is uniform. That is to say, two fault types appear everywhere within each region, but the orientation of, and the amount of deformation taken up on, each set of fault planes may vary considerably (Figure A1b). In most of the diagrams of Figure 6, style TS (major thrust faulting, strike parallel to shorter arm of cross, plus minor strike-slip faulting) or style ST (differing from style TS only in that the magnitude of strike-slip faulting is greater than that of thrust faulting) be-
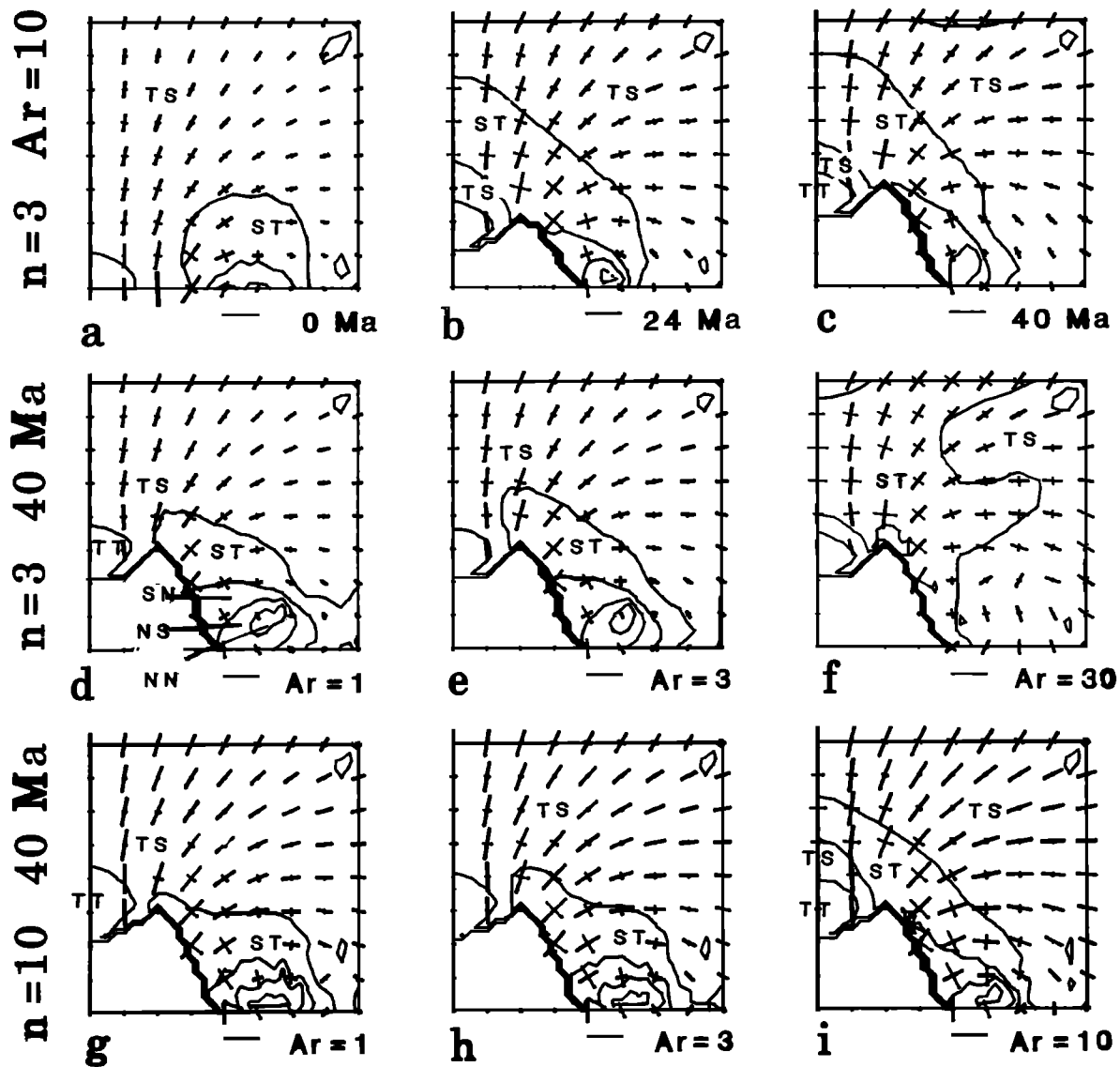
Fig. 6.   Principal horizontal stress directions for (Figures 6a–6c) $n = 3$, $Ar = 10$ and (a) $t = 0$ m.y., (b) $t = 24$ m.y., and (c) $t = 40$ m.y.; (Figures 6d–6f) $n = 3$, $t = 40$ m.y. and (d) $Ar = 1$, (e) $Ar = 3$, (f) $Ar = 30$; (Figures 6g–6i) $n = 10$, $t = 40$ m.y. and (g) $Ar = 1$, (h) $Ar = 3$, (i) $Ar = 10$. Principal stress axes are marked by thick lines if they are compressive and by thinner lines if they are extensional; the length of each line is proportional to the magnitude of the stress. The continuous lines superimposed on each plot mark the boundaries between regions having different styles of faulting; the symbols correspond to the six different regimes shown in Figure A1b: TT, thrust faulting on planes striking parallel to each principal axis; TS, thrust faulting striking perpendicular to σ_3 with minor strike-slip faulting; ST, strike-slip faulting with minor thrusting; SN, strike-slip faulting with minor normal faulting; NS, normal faulting striking perpendicular to σ_1 with minor strike slip faulting; NN, normal faulting on planes striking parallel to each principal axis (see Appendix A). Note particularly the increase in the extent of style ST faulting with time for $Ar > 3$ (Figures 6a–6c) and with Ar for fixed n (Figures 6d–6i). Regions TS and ST are indicated on each figure; regions TT, SN, NS, and NN are too small to mark clearly, but their relative positions are as shown in Figure 6d.

tween them cover most of the box. At time $t = 0$, the predominant fault style is thrusting (style TS), and this remains so at all time for calculations with $Ar \leq 1$. However, if $Ar > 1$, we see a progressive change in fault style from style TS to style ST over a large area in front of and to the side of the indenter. Figures 6a–6c show the progression in time for the case $n = 3$, $Ar = 10$; and for comparison with Figure 6c, Figures 6d–6f show the dependence of the style of faulting on Ar for $n = 3$ at 40 m.y. Figures 6g–6i show the dependence on Ar for $n = 10$ at 40 m.y. The conversion from dominant thrust faulting to dominant strike-slip faulting occurs more readily at higher Argand number because it is the resistance to further crustal thickening at large Ar that forces thrust faulting to decrease

(compare Figure 5). However, we wish to emphasize that even in cases where the thrust faulting remains dominant relative to the strike-slip faulting (e.g., along the axis of symmetry in Figure 6h), some strike-slip faulting is required to accommodate the deformation. The other regions (TT, thrust faulting parallel to both principal stresses, which occurs immediately in front of the indenter; NS and SN, strike slip plus normal faulting; and NN, both components of normal faulting, beside the indenter in the region of crustal thinning) are restricted to small areas that do not change appreciably as the deformation progresses. It should be appreciated in interpreting Figure 6 that the strain rates over large areas of the box would be too small to detect appreciable seismicity, but that the areas of

maximum strain rate (Figure 5) mainly overlap regions TS and ST.

We have so far only discussed the short-term response, assuming that there are always appropriately oriented faults to take up the deformation; however, *McKenzie and Jackson* [1983] show that if faulting in near-surface rocks is to accommodate the same strain as is experienced by an underlying viscous medium, only certain classes of finite strain result in stable faults (i.e., faults that maintain an approximately constant orientation with respect to the principal stress axes and hence will remain active). Such strains have no rotation about a vertical axis and would correspond, for example, to the region of plane strain horizontal shortening in front of the indenter (Figure 8b). We should expect thrust faulting to be a stable mode of failure here and that the faulting in such a region would thus bear a simple relation to the stress history. In contrast, where the deformation requires strike-slip faulting (such as in simple shear zones), the faults must themselves rotate and therefore will not exhibit large displacements [*McKenzie and Jackson*, 1983]. Thus because the region along the side of the indenter has a strong component of rotation about vertical axes, we should not expect one set of faults to accommodate the entire finite deformation (see Figure 8c).

Rotations. In regions where the deformation of continental lithosphere appears, on the basis of contemporary seismicity and recent fault distributions, to be diffuse on length scales greater than tens of kilometers, palaeomagnetic measurements can yield consistent rotations that are not easily related to platelike motions [e.g., *McKenzie and Jackson*, 1983; *Walcott*, 1984; *Luyendyk et al.*, 1985]. We concentrate our discussion on the finite strain and rotation results for the experiments with $n = 10$ and $Ar = 3$ and the boundary condition of Figure 1a, but except where indicated, qualitatively similar results are observed for other combinations of parameters.

The instantaneous rate of rotation about a vertical axis, equal to half the vorticity (equation (B3)), may be calculated at any material point and integrated with respect to time to give the total rotation of that point. It must be emphasized that this is the rotation that would be experienced by a rigid rotor or disc of negligibly small dimension lying on top of the deforming fluid. This rotation is different from the rotation of the material vectors that are aligned with the principal strain axes after the deformation. *McKenzie and Jackson* [1983] suggest that integrated vorticity is the appropriate measure of rotation for small crustal units in a continental collision zone, in the sense that this measure will correspond to observed changes in magnetic declination. McKenzie and Jackson's measure of rotation may be incorrect to the extent that such blocks deform internally or that their resistance to the underlying flow is sufficiently great to modify that flow. (Note that as well as the consistent rotations mentioned above, there are also regions where individual crustal blocks appear to dominate the deformation [e.g., *Jackson and McKenzie*, 1984; *Ron et al.*, 1984].)

Figure 7a shows the rotations calculated for the case in which $n = 10$ and $Ar = 3$. The vorticity boundary conditions assure a nearly irrotational flow in front of the indenter ($u = \partial v/\partial x = 0$ on the axis of symmetry) and strong rotation about vertical axes along the side of the indenter, where clockwise rotations of about 90° are seen. These rotations, and the rotation of the boundary itself, result from the dextral shear that the velocity profile (Figure 1) imposes. The magnitude of the rotations in the region beside the indenter varies inversely as the width of the shear zone across which the indenting velocity is assumed to fall to zero and hence is strongly dependent on our assumptions about the boundary velocity distri-

bution during the collision. Apart from the region near $y = D$, rotations that would be detectable palaeomagnetically ($\gtrsim 10°$) are confined to a region within about 1000 km of the indenter.

For each set of boundary conditions (Figure 1), small clockwise rotations of order 10° are calculated on the northeast part of the plateau. For the arcuate indenter (Figures 1b and 7a) we also show similarly small anticlockwise rotations in the southeast part of the plateau, adjacent to the indenter (directions used here assume that $+y$ is north). The rotations have the opposite sign in the left of half of the solution, not shown in Figure 7.

Figure 7b shows the corresponding rotations for $n = 3$ and $Ar = 30$, which differ from those of Figure 7a in that the region of significant rotations covers a greater area around the indenter and a region of generally smaller anticlockwise rotations appears next to the boundary $y = D$. The latter rotations result from flow in the $+x$ direction relative to the rigid northern boundary, but they are generally negligible for $n > 3$ unless the Argand number is large.

Finite strain. The uncertainty involved in relating the calculated finite strains to the strains that might be inferred from observations made in old orogenic belts is similar to that involved in relating seismicity to strain rate fields (above). Even in the ductile field, deformation may still be concentrated into relatively narrow shear zones that represent anisotropy and inhomogeneity [e.g., *Ramsay*, 1980], and the difficulties involved in determining a regional strain in a section of old orogen may be prohibitive. We discuss briefly the finite strains that we calculate, although we recognize that the scale at which we make these calculations (100–200 km) is considerably larger than the scale at which it is commonly feasible to estimate strain from field observations.

Figure 8a shows horizontal sections through representative finite strain ellipsoids (Appendix B) calculated with the boundary conditions of Figure 1a and with $n = 10$ and $Ar = 3$, at 8-m.y. intervals from $t = 0$ to $t = 40$ m.y. Because of the assumption that one principal stress is vertical, the maximum and minimum horizontal strains are principal strains; the third principal strain is proportional to the crustal thickness.

Near the axis of symmetry the deformation is nearly irrotational and can be regarded as close to progressive pure shear; after 40 m.y., Figure 8b has a compressional strain axis close to the y direction with an elongation of 0.5 and vertical extension (crustal thickening) by a factor of 2.0. The strain rates for this element decrease monotonically as the crust is thickened and begins to resist further thickening; as can be seen from the magnitude of the strain rate axes and the progressive deformation of the ellipse, almost half of the total deformation (at $t = 40$ m.y.) is accomplished in the first 8 m.y.

Stronger deformation is found near the corner and along the sides of the indenter (Figure 8c), but we interpret the results in these regions with the caveat that the deformation there is strongly influenced by the details of the indenting boundary condition. Figure 8c undergoes approximately progressive pure shear during the first 16 or 20 m.y., during which time the magnitude of the compressive strain rate almost doubles. However, during the remainder of the deformation, the material vectors that are initially aligned with the principal strain rate axes rotate rapidly with respect to the instantaneous principal strain rate axes, so that after 40 m.y. the material vector that was initially parallel to the compressive principal strain rate axis is at an angle of 61° from the instantaneous maximum strain rate axis; the vector originally parallel to the tensional principal strain rate axis is now at an angle of 28° from the instantaneous tensional principal strain rate axis. Lines originally corresponding to thrust faults would, at 40
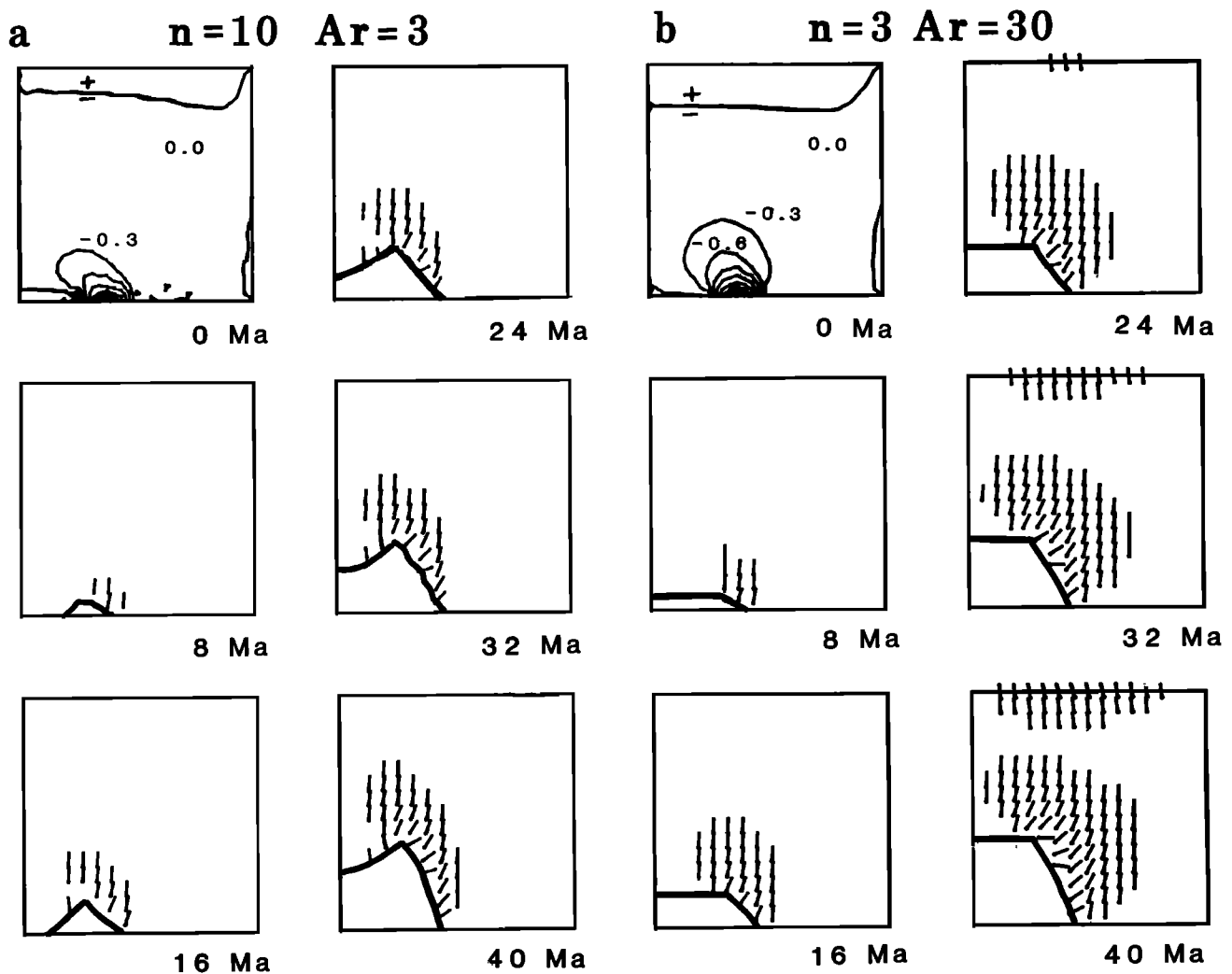
a   n = 10   Ar = 3

b   n = 3   Ar = 30

Fig. 7. (a) For boundary conditions of Figure 1b and n = 10 and Ar = 3 and (b) boundary conditions of Figure 1a and n = 3 and Ar = 30, contours of instantaneous rotation rate at time zero, and net rotation at discrete points in the deforming medium at later times. The angle between the small bar and the y axis is the total rotation. Only rotations greater than 5° are shown. The contour interval for rotation rate is 1.59 × 10⁻¹⁶ rad/s (0.3°/m.y.). Some of the contours are labeled, and the others can be identified easily as the rotation rate is increasingly negative (clockwise) as the velocity ramp on the indenter boundary is approached.

m.y., be more favorably oriented to take up strike-slip faulting. During the 40 m.y., the increase in the tensile strain rate relative to the compressive strain rate implies a major change in the style of faulting. Decomposing the strain rate matrix into two orthogonal double couples (see Appendix A) shows that at $t = 0$ the rate of moment release for thrust faulting is approximately 3–4 times greater than the rate for strike-slip faulting. In contrast, at $t = 40$ m.y. the rate of moment release for strike-slip faulting is about 13 times that of thrust faulting. The transition from dominant thrust faulting to dominant strike-slip faulting for this element occurs between 16 and 24 m.y., although both components are present throughout the deformation.

Figure 8a also illustrates the absolute and relative latitudinal displacements of the points at the centers of the ellipses. Further discussion of the latitudinal displacements in the context of the India-Asia collision is presented by England and Houseman [this issue].

4. CONCLUSIONS

We have presented calculations of crustal thickness distributions, stress, strain, and strain rate fields and of latitudinal displacements and finite rotations from a model for continental collision that treats the lithosphere as a thin viscous layer subject to indenting boundary conditions. The finite rotation is not very sensitive to rheological parameters (Figure 7), and the finite strain may be impossible to determine on the scale that we calculate, but we discuss these features of deformation in section 3.3 for the light that such calculations may throw on the deformation in regions with a complex strain history in which rotation is an important component of the deformation.

The results of this paper support the conclusions of England and McKenzie [1982] regarding the role of gravity in governing the deformation of a thin viscous layer subject to indenting boundary conditions. When gravitational forces are less than the forces from the boundary conditions, that is at short times, or for Argand numbers less than approximately one, the length scale of the deformation is determined by the dominant wavelength of the indenting boundary condition [England et al., 1985], and the deformation in front of the indenting boundary is taken up almost entirely by irrotational lithospheric shortening. However, for $Ar < 1$ the across-strike length scale of the deformation is sufficiently short that crustal
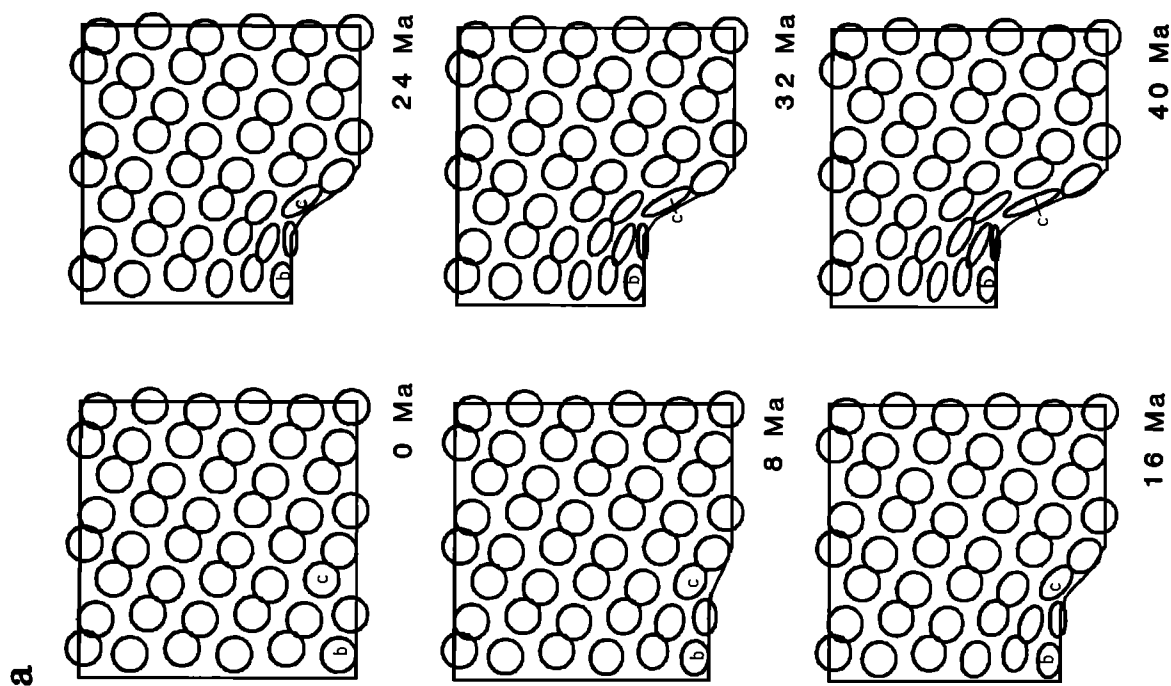
Fig. 8. (a) Finite strain ellipses for $n = 10$ and $Ar = 3$ with the boundary conditions of Figure 1a at times given in million years after the start of the collision. The lengths of the collision. The lengths of the major and minor axes are proportional to the principal elongations. Each ellipse is calculated from the total deformation of a given triangular element, relative to its initial shape and size. To avoid crowding, ellipses are only shown for approximately one sixth of the total number of elements. (b) and (c) The finite strain ellipses for the two elements labeled in Figure 8a are plotted together with instantaneous principal strain rates and the material vectors (arrows) that at $t = 0$ are of unit length and coincide with the principal strain rate axes. The principal strain rates are shown as elongated triangles with apex to center for compressive strain, apex out for tensile strain; lengths of the triangles are proportional to the strain rates. The maximum compressive strain rate at $t = 0$ is 1.12×10^{-15} s^{-1} (Figure 8b) and 0.71×10^{-15} s^{-1} (Figure 8c).

thicknesses (and topographic heights) far greater than those observed in Asia are generated after convergence of 2000 km.

At higher Argand numbers the deformation described here differs from the results of *England and McKenzie* [1982] and those of previous workers who have neglected vertical strain [e.g., *Tapponnier and Molnar*, 1976] and/or buoyancy forces [*Vilotte et al.*, 1982]. The thickening is accommodated by the formation of a plateaulike region in front of the indenter, whose width and height and the steepness of whose edges are sensitive to both the stress-strain exponent *n* and the Argand number (Figure 4). In order for this plateau to be of approximately the same crustal thickness as the Tibetan plateau (50–70 km after 2000 km of convergence), *n* must be 3 or more and the Argand number must be between about 1 and 10. Under these conditions, gravity plays an important role in the deformation of the sheet and gives a distinctive form to the strain rate field: Figure 6 shows that while crustal thickening and thrust faulting dominate in the early stages of the deformation, buoyancy forces increase as the crust thickens; strike-slip faulting becomes more important and may dominate over thrust faulting over large parts of the deforming region (see also *England* [1982]), and the locus of maximum vertical strain rate (thickening) migrates away from the indenter and lies on the downslope of the plateau, while the plateau itself occupies a local minimum in the strain rate field (Figure 5).

A companion paper [*England and Houseman*, this issue] compares the results of calculations using this model against topographic, seismic, and palaeomagnetic observations in the India-Asia collision zone.

APPENDIX A: STYLE OF FAULTING AND RATE OF MOMENT RELEASE IN THE UPPER CRUST SUBJECT TO A SPECIFIED STRAIN RATE TENSOR

We consider the behavior of the uppermost crust in response to the deformation of the underlying continental lithosphere; it has been assumed explicitly in this paper, and in others describing continental deformation in continuum mechanics terms, that the brittle upper crust follows passively the deformation of its viscous substrate; i.e., the strain rate tensor, $\dot{\varepsilon}$, in the upper crust is the same as that of the depth-averaged lithosphere below, over a span of time that is long compared with earthquake repeat times and short compared with the times for appreciable changes to occur in the strain rate field. We shall also assume that the upper crust contains many randomly oriented faults so that if a sufficiently large volume is considered, it is isotropic and homogeneous.

After aligning the *x*, *y*, and *z* axes with the principal strain rate directions, $\dot{\varepsilon}$ can be written in the form

$$\dot{\varepsilon} = \begin{bmatrix} \dot{\varepsilon}_x & 0 & 0 \\ 0 & \dot{\varepsilon}_y & 0 \\ 0 & 0 & \dot{\varepsilon}_z \end{bmatrix} \qquad (A1)$$

where $\dot{\varepsilon}_x + \dot{\varepsilon}_y + \dot{\varepsilon}_z = 0$ and $\dot{\varepsilon}_x$ and $\dot{\varepsilon}_y$ are the principal horizontal strain rates. We assume that the brittle portion of the crust deforms by slip on faults and hence that $\dot{\varepsilon}$ may be expressed as a sum of double couples, each double couple corresponding to two conjugate active fault systems. It is apparent that $\dot{\varepsilon}$ can be written as the sum of three orthogonal double couples:

$$\begin{bmatrix} \dot{\varepsilon}_x & 0 & 0 \\ 0 & \dot{\varepsilon}_y & 0 \\ 0 & 0 & \dot{\varepsilon}_z \end{bmatrix} = \begin{bmatrix} e & 0 & 0 \\ 0 & -e & 0 \\ 0 & 0 & 0 \end{bmatrix} + \begin{bmatrix} \dot{\varepsilon}_x - e & 0 & 0 \\ 0 & 0 & 0 \\ 0 & 0 & e - \dot{\varepsilon}_x \end{bmatrix}$$
$$+ \begin{bmatrix} 0 & 0 & 0 \\ 0 & \dot{\varepsilon}_y + e & 0 \\ 0 & 0 & -\dot{\varepsilon}_y - e \end{bmatrix} \qquad (A2)$$

corresponding to a strike-slip component plus two components that may be either thrust or normal, depending on the signs of the nonzero elements. However, to determine the constant *e*, and hence the relative magnitude of these three components, we need to consider the state of stress within the brittle layer.

Brace and Kohlstedt [1980] summarize the arguments for believing that stresses in the upper part of the lithosphere are governed by Byerlee's law [*Byerlee*, 1968] which relates the shearing stress σ_s at which frictional resistance is overcome on a fault to the effective normal stress $\bar{\sigma}_n$ on the fault:

$$|\sigma_s| = c - \mu\bar{\sigma}_n \qquad (A3)$$

where μ and c depend on the magnitude of $\bar{\sigma}_n$. We shall assume that the effective normal stress is related to the normal stress σ_n and the pore fluid pressure σ_p by

$$\bar{\sigma}_n = \sigma_n - \sigma_p \qquad (A4)$$

If we consider the three independent pairs of principal stress axes, equation (A3) gives six possible states of stress (Figure A1a) for which the material will yield, two for strike-slip faulting on vertical planes at an angle $(1/2)\tan^{-1}(1/\mu)$ to the principal compressive stress axis:

$$(\sigma_y - \sigma_z) = \left[\frac{(1 + \mu^2)^{1/2} \pm \mu}{(1 + \mu^2)^{1/2} \mp \mu}\right](\sigma_x - \sigma_z) \pm 2\left[\frac{\mu(\sigma_z - \sigma_p) - c}{(1 + \mu^2)^{1/2} \pm \mu}\right]$$
$$(A5a)$$

two for normal faulting:

$$(\sigma_\alpha - \sigma_z) = 2\left[\frac{c - \mu(\sigma_z - \sigma_p)}{(1 + \mu^2)^{1/2} + \mu}\right] \qquad (A5b)$$

where α is the maximum principal stress direction and the fault planes strike parallel to the intermediate stress axis and dip $(90° - (1/2)\tan^{-1}(1/\mu))$, and last, two for thrust faulting:

$$(\sigma_\alpha - \sigma_z) = 2\left[\frac{\mu(\sigma_z - \sigma_p) - c}{(1 + \mu^2)^{1/2} - \mu}\right] \qquad (A5c)$$

where α is the minimum principal stress direction and the fault planes strike parallel to the intermediate stress axis and dip $(1/2)\tan^{-1}(1/\mu)$.

As Figure A1a shows, at most two of the above six conditions can be satisfied simultaneously, so at most two of the double couples in (A2) may be nonzero, and the only permissible combination of fault type are normal faults on two orthogonal planes, thrust faults on two orthogonal planes, thrust plus strike slip or normal plus strike slip. Since one of the double couples must vanish, possible values of *e* are: 0, $\dot{\varepsilon}_x$ or $-\dot{\varepsilon}_y$.

If the original strain rate tensor (A1) is a double couple, the solution is trivial, though the stress field is indeterminate to the extent that it is only constrained to lie on the appropriate boundary segment of the hexagon in Figure A1a. In general, however, the stress field in the plastic layer must be described by one of the six vertices of the hexagon. For vertex A, it is clear that $e = 0$ since the strike-slip feature criterion is not met, and (since $\dot{\varepsilon}_x < 0$ and $\dot{\varepsilon}_y < 0$) the corresponding strain rate field may be anywhere in quadrant TT of Figure A1b. Similarly, sectors TS and ST in the $(+\dot{\varepsilon}_x, -\dot{\varepsilon}_y)$ quadrant of the strain rate field correspond to vertex B of the stress field, and $e = \dot{\varepsilon}_x$ in (A2) since only the criteria for strike slip and *y* direction compression are satisfied. It may be verified by checking the other four vertices that *e* in equation (A2) should be set to the median value of $(0, \dot{\varepsilon}_x, -\dot{\varepsilon}_y)$. In Figure A1b the strain rate fields corresponding to each of vertices B, C, E, and F are subdivided into two regions, depending on whether the mag-
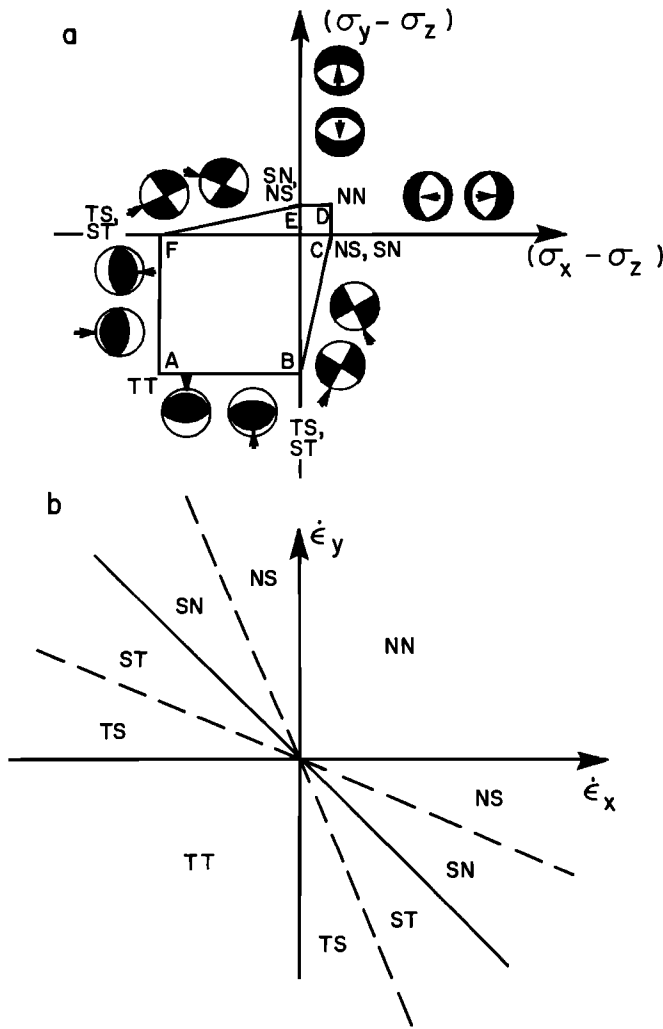
Fig. A1. (a) Yield envelope in the $(\sigma_x - \sigma_z) - (\sigma_y - \sigma_z)$ plane of the material described by equations (A3) and (A4) with $\mu = 0.85$; the lines BC, FE, ED, DC, FA, and AB are described by equations (A5a)-(A5c), respectively. On each boundary segment, failure is permitted on either of the arrowed planes shown by the two lower hemisphere projections (indicating the focal mechanism that would be observed if this failure took the form of earthquake activity). At the vertices of the hexagon, failure can occur on the four different planes appropriate to the two intersecting boundary segments. The mnemonics SN, NN, etc., at each vertex show the two permissible styles of deformation (S, strike-slip; T, thrust; N, normal), and the correspondence of that vertex with the regions in strain rate space shown in Figure A1b. (b) Any given strain rate tensor lies in one of the six regions of the $(\dot{\varepsilon}_x - \dot{\varepsilon}_y)$ plane shown. Each region is associated with the stress field defined at one of the vertices of Figure A1a. The dashed lines separate fields in which strike-slip failure dominates the deformation (ST and SN) from those in which reverse (TT and TS) and normal (NN and NS) failure dominate. These correspond, respectively, to regions in which σ_2, σ_1, and σ_3 are vertical and would, if stresses were assumed proportional to strain rate, correspond to regions in which Anderson's [1951] criterion predicts only strike-slip, reverse, or thrust faulting in a brittle medium.

nitude of the strike-slip component is greater or less than the magnitude of the accompanying thrust or normal faults.

Because there are two conjugate fault planes for each of the six equations (5a)–(5c), there are four distinct fault mechanisms possible at each vertex of the stress hexagon, and there might appear to be considerable variation of the local orientation of the stress axes inferred from a group of fault plane solutions. In general, the orientations of the T, null, and P axes from focal mechanisms of individual events accommodating deformation corresponding to one of the vertices of Figure

A1a will not be identical to the σ_1, σ_2, and σ_3 axes in the underlying viscous sheet. For example, the P and null axes of the focal mechanisms that are permitted at vertex A in Figure A1a may lie as far as 90° from the corresponding (σ_3 and σ_2) axes in the underlying fluid. In contrast, the T axis of each of the events at vertex A is only $(45° - (1/2) \tan^{-1} (1/\mu))$ from the vertical σ_1 axis, and the average of the four lies along the σ_1 axis.

For vertices A, C, and E, the T axis shows approximately constant orientation and is aligned with the σ_1 direction, while for vertices B, D, and F the P axis is approximately constant in orientation and aligned with the σ_3 direction.

For each of the two double couples describing the strain rate tensor, consistency of the above argument requires that slip occurs on the two conjugate sets of fault planes with equal magnitude, a condition that is probably not met where there is a strong fabric to the crust. The relative magnitude of the two double couples is determined only by the relative magnitudes of $\dot{\varepsilon}_x$, $\dot{\varepsilon}_y$, and $\dot{\varepsilon}_z$. Finally, each of the double couples is associated with a rate of moment release per unit volume V [Molnar, 1983]

$$\frac{1}{V}\frac{dM}{dt} = 2m(1 + \mu^2)^{1/2}|\dot{\varepsilon}| \tag{A6}$$

where m is the shear modulus and $|\dot{\varepsilon}|$ is the magnitude of the nonzero components of the double-couple tensor.

APPENDIX B: FORMULATION AND MEANS OF SOLUTION

The dimensionless governing equations for the deformation of a thin viscous sheet having a power law rheology given by equation (3) are derived from (1) following England and Mc-Kenzie [1982]:

$$\frac{\partial}{\partial x_\beta}\left[\eta\left(\frac{\partial u_\alpha}{\partial x_\beta} + \frac{\partial u_\beta}{\partial x_\alpha}\right)\right] + \frac{\partial}{\partial x_\alpha}\left[2\eta\left(\frac{\partial u}{\partial x} + \frac{\partial v}{\partial y}\right)\right] = Ar\frac{\partial S^2}{\partial x_\alpha} \tag{B1}$$

$$\alpha, \beta = 1, 2$$

and from equation (2)

$$\frac{1}{S}\frac{\partial S}{\partial t} = -\left(\frac{\partial u}{\partial x} + \frac{\partial v}{\partial y}\right) \tag{B2}$$

The definition of the Argand number (equation (6)) is determined by the following choice of dimensionless variables for time t, crustal thickness S, horizontal coordinates (x, y), and velocities in the x and y directions (u, v):

$$t = (V_0/L)t'$$
$$(x, y, S) = (x', y', S')/L \tag{B3}$$
$$(u, v) = (u', v')/V_0$$

where L is the sheet thickness and V_0 is a reference velocity (see Table 1); the dimensional variables are primed. The dimensionless viscosity η is defined by

$$\eta = (\dot{E}L/V_0)^{1/n - 1} \tag{B4}$$

where $\dot{E}$ is the second invariant of the dimensional strain rate tensor (equation (5)).

We define the finite rotation θ (following McKenzie and Jackson [1983]) as the angle through which a small rigid horizontal plate, on top of the deforming medium, is rotated. At any point the instantaneous rate of rotation is equal to half the vorticity:

$$\frac{\partial \theta}{\partial t} = \frac{1}{2}\left(\frac{\partial v}{\partial x} - \frac{\partial u}{\partial y}\right) \tag{B5}$$

The total rotation that any material point in the fluid has undergone is then evaluated by numerical integration with

respect to time of (B3), with the initial condition $\theta = 0$ for $t = 0$.

To solve the coupled equations (B1) and (B2), the solution domain is divided into triangular elements, as shown in Figures 1a and 1b. Each element has six nodes, its vertices and the midpoints of its sides.

We use a quadratic interpolation on the velocity field with the Galerkin finite element approximation [e.g., Huebner, 1965; Zienkiewicz, 1977] to transform (B1) into the matrix form

$$\begin{bmatrix} K^1 & K^2 \\ (K^2)^T & K^4 \end{bmatrix} \begin{bmatrix} u \\ v \end{bmatrix} = \begin{bmatrix} a \\ b \end{bmatrix} \qquad (B6)$$

[cf. Bird and Piper, 1980; Bird and Baumgardner, 1984]. The four component matrices of (B6) are each $N \times N$ matrices, where N is the number of nodes (595 for the mesh of Figure 1). The matrix elements were calculated using a seven point numerical integration scheme for triangles [Huebner, 1975, p. 421], which is accurate to sixth order.

If the fluid has a Newtonian viscosity ($n = 1$ in (3)), (B6) is linear in the velocity variables u and v. However, for non-Newtonian flow ($n > 1$), an iterative scheme is necessary; the matrix elements must be recalculated using the velocity field from the previous iteration. For $n = 3$, convergence typically requires five iterations. For a given configuration and crustal thickness distribution a solution for the velocity field is obtained, and new mesh conditions, crustal thicknesses, and finite rotations are then calculated by a simple first-order finite difference approximation.

The size of the time step Δt was chosen to place an arbitrary upper bound on the maximum deformation of any element in time Δt:

$$\Delta t \left(\left| \frac{\partial u}{\partial x} \right| + \left| \frac{\partial v}{\partial y} \right| \right)_{max} \lesssim 10\% \qquad (B7)$$

In several tests, repeat runs were carried out with the time step reduced by a factor of 2. Convergence of the different solutions showed that the simple first-order time-stepping scheme is satisfactory and that (B7) is an adequate restriction on the size of the time step. Repeat runs with a coarser element mesh (approximately 4 times fewer nodes) also showed that the mesh resolution of Figure 1 is adequate for the experiments. Solutions at time zero with the boundary condition of Figure 1a agreed with finite difference solutions obtained by England and McKenzie [1982] to better than 2%.

At time t the ellipsoid of finite deformation can be calculated with reference to the initial conditions. We calculate the components of strain from the initial and final coordinates of the element vertices, and they thus represent an average over the element of the deformation gradient tensor [Malvern, 1969, pp. 155–156]. In addition, one principal strain rate is always vertical, so the strain ellipsoid can be represented by a horizontal section through it that contains two of the principal strain axes.

REFERENCES

Anderson, E. M., The Dynamics of Faulting, 206 pp., Oliver and Boyd, Edinburgh, 1951.
Ashby, M. F., and R. A. Verrall, Micromechanisms of flow and fracture, and their relevance to the rheology of the upper mantle, in The Creep of Engineering Materials, and of the Earth, Royal Society, London, 1978.
Bird, P., and J. Baumgardner, Fault friction, regional stress, and crust-mantle coupling in southern California from finite-element models, J. Geophys. Res., 89, 1932–1944, 1984.
Bird, P., and K. Piper, Plane stress finite element models of tectonic flow in southern California, Phys. Earth Planet. Inter., 21, 158–175, 1980.
Brace, W. F., and D. L. Kohlstedt, Limits on lithospheric stress imposed by laboratory experiments, J. Geophys. Res., 85, 6248–6252, 1980.
Byerlee, J. D., Brittle-ductile transition in rocks, J. Geophys. Res., 73, 4741–4750, 1968.
England, P. C., Some numerical investigations of large scale continental deformation, in Mountain Building Processes, edited by K. Hsu, Academic, Orlando, Fla., 1982.
England, P. C., and G. A. Houseman, Finite strain calculations of continental deformation, 2, Application to the India-Asia collision zone, J. Geophys. Res., this issue.
England, P. C., and D. P. McKenzie, A thin viscous sheet model for continental deformation, Geophys. J. R. Astron. Soc., 70, 295–321, 1982. (Correction to "A thin viscous sheet model for continental deformation," Geophys. J. R. Astron. Soc., 73, 523–532, 1983.)
England, P. C., G. A. Houseman, and L. Sonder, Length scales for continental deformation in convergent, divergent, and strike-slip environments: Analytical and approximate solutions for a thin viscous sheet model, J. Geophys. Res., 90, 3551–3557, 1985.
Goetze, C., The mechanisms of creep in olivine, Philos. Trans. R. Soc. London, Ser. A, 288, 99–119, 1978.
Huebner, K. H., The Finite Element Method for Engineers, John Wiley, New York, 1975.
Jackson, J. A., and D. P. McKenzie, Active tectonics of the Alpine—Himalayan belt between western Turkey and Pakistan, Geophys. J. R. Astron. Soc., 77, 185–264, 1984.
Luyendyk, B. P., M. J. Kumerling, R. R. Terres, and J. S. Hornafius, Simple shear of southern California during Neogene time suggested by paleomagnetic declinations, J. Geophys. Res., 90, 12,454–12,466, 1985.
Malvern, L. E., Introduction to the Mechanics of Continuous Medium, Prentice-Hall, Englewood Cliffs, N. J., 1969.
McKenzie, D. P., Can plate tectonics describe continental deformation?, in Structural History of the Mediterranean Basins, edited by B. Biju-Duval and L. Montadert, pp. 189–196, Editions Technip, Paris, 1976.
McKenzie, D. P., and J. Jackson, The relationship between strain rates, crustal thickening, paleomagnetism, finite strain and fault movements within a deforming zone, Earth Planet. Sci. Lett., 65, 182–202, 1983.
Molnar, P., Average regional strain due to slip on numerous faults of different orientations, J. Geophys. Res., 88, 6430–6432, 1983.
Molnar, P., and P. Tapponnier, Cenozoic tectonics of Asia: Effects of a continental collision, Science, 189, 419–426, 1975.
Molnar, P., T. J. Fitch, and F. T. Wu, Fault plane solutions of shallow earthquakes and contemporary tectonics in Asia, Earth Planet. Sci. Lett., 19, 101–112, 1973.
Ramsay, J. G., Shear zone geometry: A review, J. Struct. Geol., 2, 83–99, 1980.
Ron, H., R. Freund, Z. Garfunkel, and A. Nur, Block rotation by strike-slip faulting: Structural and palaeomagnetic evidence, J. Geophys. Res., 89, 6256–6270, 1984.
Sonder, L. J., and P. C. England, Vertical averages of rheology of the continental lithosphere: Relation to thin sheet parameters, Earth Planet. Sci. Lett., in press, 1986.
Tapponnier, P., and P. Molnar, Slip-line field theory and large-scale continental tectonics, Nature, 264, 319–324, 1976.
Vilotte, J. P., M. Diagnieres, and R. Madariaga, Numerical modeling of intraplate deformation: Simple mechanical models of continental collision, J. Geophys. Res., 87, 10709–10728, 1982.
Walcott, R., The kinematics of the plate boundary zone through New Zealand: A comparison of short- and long-term deformation, Geophys. J. R. Astron. Soc., 79, 613–633, 1984.
Zienkiewicz, O. C., The Finite Element Method, McGraw-Hill, New York, 1977.

P. England, Department of Geological Sciences, Harvard University, Hoffman Laboratory, 20 Oxford Street, Cambridge, MA 02138.
G. Houseman, Research School of Earth Sciences, Australian National University, Canberra ACT 2601, Australia.